



# Investigation of non-ideal gas flows around a circular cylinder

Camille Matar, Paola Cinnella, Xavier Gloerfelt, Felix Reinker, Stefan Aus Der Wiesche

## ► To cite this version:

Camille Matar, Paola Cinnella, Xavier Gloerfelt, Felix Reinker, Stefan Aus Der Wiesche. Investigation of non-ideal gas flows around a circular cylinder. Energy, In press, pp.126563. 10.1016/j.energy.2022.126563 . hal-03940146

**HAL Id: hal-03940146**

**<https://hal.science/hal-03940146>**

Submitted on 15 Jan 2023

**HAL** is a multi-disciplinary open access archive for the deposit and dissemination of scientific research documents, whether they are published or not. The documents may come from teaching and research institutions in France or abroad, or from public or private research centers.

L'archive ouverte pluridisciplinaire **HAL**, est destinée au dépôt et à la diffusion de documents scientifiques de niveau recherche, publiés ou non, émanant des établissements d'enseignement et de recherche français ou étrangers, des laboratoires publics ou privés.

# Investigation of non-ideal gas flows around a circular cylinder

Camille Matar<sup>a</sup>, Paola Cinnella<sup>a</sup>, Xavier Gloerfelt<sup>b</sup>, Felix Reinker<sup>c</sup>, Stefan aus der Wiesche<sup>c</sup>

<sup>a</sup>*Sorbonne Université, Institut Jean Le Rond d'Alembert, Paris, France*

<sup>b</sup>*Arts et Métiers Institute of Technology, Laboratoire DynFluid, Paris, France*

<sup>c</sup>*FH Münster, Department of Mechanical Engineering, Steinfurt, Germany*

---

## Abstract

The aerodynamic performance of a cylinder Pitot probe for velocity measurements in compressible non-ideal gas flows, such as those encountered in Organic Rankine Cycle (ORC) turbines, is investigated by means of Computational Fluid Dynamics. Numerical simulations are performed at subsonic and transonic conditions, and freestream Reynolds numbers are in the cylinder critical regime. The working fluid is the organic vapor Novec<sup>TM</sup>649. Air flow simulations at similar inlet conditions are reported for comparison. Steady and unsteady RANS solutions are computed with the Spalart-Allmaras turbulence model. The results are assessed against experimental measurements collected in a wind tunnel. URANS is in good agreement with experimental data for all considered conditions, and delivers reasonably accurate estimations of the cylinder back pressure. Using a dense gas leads to a lower minimum pressure coefficient compared to air, alongside a reduced maximum Mach number due to the non-ideal speed of sound behaviour. In the experimentally studied range of compressibility factors and Mach numbers, discrepancies observed with respect to air flow are mostly an effect of the different isentropic exponents. In the transonic regime, shock waves causing boundary layer separation are weakened in the dense gas, but back pressure is also decreased, contributing to rising form drag.

*Keywords:* Non-ideal gas, transonic, cylinder, Pitot probe, RANS

---

## 1. Introduction

In recent years, the study of dense-gas dynamics has received increased attention, due to manifold applications in Engineering. One of the most important ones is the design of improved turbine expanders for Organic Rankine Cycle (ORC) power plants [1, 2]. On the one hand, such components work in the transonic to supersonic flow regimes, due to high pressure ratios and generally low speed of sound of the working fluid. This may lead to strong compressibility effects resulting in process efficiency losses. On the other hand, the flow can be optimized to reduce these losses, as well as the choice of working fluid. Dense-gas are molecularly complex and the energy associated with the rotation, vibration or collision between molecules cannot be neglected, unlike air even at typical Rankine cycle machine operating conditions. This in turn increases their density to typically one order of magnitude higher than that of a calorically and thermally perfect gas (PFG). Dense-gas dynamics can be described by using the fundamental derivative of gas dynamics [3]:

$$\Gamma := \frac{v^3}{2c^2} \frac{\partial^2 p}{\partial v^2} \Big|_s = 1 + \frac{\rho}{c} \frac{\partial c}{\partial \rho} \Big|_s \quad (1)$$

which indicates how the speed of sound  $c = \sqrt{(\partial p / \partial \rho)_s}$  varies with density  $\rho = 1/v$  through isentropic processes, where  $v$  is the specific volume,  $p$  is the pressure and  $s$  is the entropy. Close to the saturation curve, a region where  $\Gamma < 1$  may exist, which implies that the rate of change of speed of sound with respect to density,  $(\partial c / \partial \rho)_s$ , is negative. Therefore,  $c$  drops through compressions and grows through expansions. This in turn lowers the local Mach number, hence reducing the probability of shock wave formation, as well as their strength. It is clear that ORC machines can benefit from this behaviour [4]. Note that for a PFG, expression (1) reduces to  $\Gamma = (\gamma + 1)/2$ , where  $\gamma = c_p/c_v$  is the specific heat capacity ratio. This implies that

$\Gamma > 1$  for a PFG, so that  $c$  decreases during expansions, while the Mach number increases monotonically. Now, inspecting the change of entropy through a weak shock [5]:

$$\Delta s = -\frac{c^2 \Gamma}{v^3} \frac{\Delta v^3}{6T} + \mathcal{O}(\Delta v^4), \quad (2)$$

$T$  being the temperature. We see that, for  $\Gamma \ll 1$ , the change in entropy is diminished. This further reduces efficiency losses in ORC machines in the case of transonic flow. Due to the peculiar fluid properties and operating conditions, very few experimental facilities are available to characterize such dense-gas effects on turbine flow dynamics. A good example of experimental effort to provide such dataset is the study by Baumgartner *et al.* [6], who used a transient wind tunnel that enables annular cascade testing with a wide range of working fluids and operating conditions. Only global flow characterization are generally possible and Computational Fluid Dynamics (CFD) remains the main tool to investigate dense-gas flow phenomena. A challenging issue for CFD is the high characteristic Reynolds numbers encountered in dense-gas conditions, the high molar mass of organic vapors leading to densities one or two orders of magnitude higher than that of air. A good compendium of 2D/3D numerical simulations of ORC rotors/turbines flows is given in Otero *et al.* [7] (and references therein). All simulations are based on Reynolds Averaged Navier-Stokes (RANS) models using either commercial software or in-house finite-volume codes. CFD is of utmost importance to provide design guidelines [8] and to optimize turbine expander efficiency [9, 10], and can also be used to explore new operating conditions [4].

The validation of CFD solvers for dense-gas flows is a necessary step that requires experimental databases for simple canonical flows. A good example of such effort are the nozzle flow [11] and diamond-shaped airfoil [12] experiments from the Test-Rig for Organic VApours (TROVA), which served to validate the SU2 code supplemented with suitable thermodynamic models for organic fluids [13]. These simplified configurations represent elementary bricks useful to understand the inviscid behavior of ORC turbines, *e.g.* the converging-diverging nozzle being representative of ORC supersonic stators and the diamond-shaped airfoil mimicking the oblique shock interactions in turbine rotors, respectively. Another very important flow phenomenon is vortex shedding in the viscous wake of bluff trailing edges of turbine blades [14, 15], affecting the base pressure distribution around the trailing edge, wake mixing and, in the end, losses. The flow past a cylinder constitutes a good prototype to study wake dynamics, and consequently a good experimental/numerical benchmark case to assess the predictive capabilities of dense-gas flow solvers. The flow around a cylinder has been widely studied over a large range of Reynolds numbers, and to some extent for a range of high-subsonic Mach numbers [16, 17, 18, 19]. However, the available literature is focused on the ideal gas flow of air, neglecting real gas effects which are investigated in the present study. Understanding how the real-gas behaviour affects the flow around the cylinder is expected to provide indications on round trailing edge flow, and specifically losses generated in the wake.

An experimental campaign was conducted recently in the Closed LOop Wind Tunnel (CLOWT) facility at Münster University [20], using a small diameter cylinder, which is the section of a rotatable Pitot probe in the crossflow of an organic vapor (Novec™649) and of air over the low subsonic ( $M < 0.4$ ) and mid to high subsonic ( $0.4 < M < 0.8$ ) speed range. Rotatable cylinder Pitot probes can be used for total pressure measurements in Organic Rankine Cycle (ORC) turbines [21]. Their performance may be subject to the thermodynamic behaviour of the gas, if it differs from that of a PFG. It is therefore of interest to understand, if any, how the real-gas behaviour affects the flow around the tube. Time-averaged pressure measurements gave information on surface pressure distributions, and the corresponding drag and base pressure coefficients were obtained. The new results for the organic vapor flow were in reasonable agreement with literature data for air, with some deviations attributed to Reynolds number effects or experimental uncertainties. These deviations were of the same order as the scattering of the literature data, leading to the conclusion that non-ideal gas effects were of minor importance for the overall flow behaviour at the considered Mach number range. It must be noted that, due to wind tunnel constraints and to the high density of the working fluid, a very small cylinder with a diameter of 5 mm was tested. At such small dimensions, the geometry exhibited machining flaws, resulting in geometrical uncertainties (see [20]). Geometrical imperfections had an impact on the transition point in the very sensitive range of considered Reynolds numbers ( $1.5 \times 10^5 \leq Re_D \leq 6.1 \times 10^5$ ;  $Re_D = \frac{\rho_{in} U_{in} D}{\mu_{in}}$ , with  $\rho_{in}$  and  $U_{in}$  the inlet density and

velocity, respectively,  $D$  the cylinder diameter and  $\mu_{in}$  the inlet viscosity), encompassing the drag crisis and, consequently, on the measured wall pressure coefficient.

To remove such uncertainty and to provide a useful complement to the experiments, the aim of the present study is to simulate dense-gas flows over the probe, modelled as a two-dimensional circular cylinder. For that purpose, we solve the compressible Navier-Stokes equations supplemented by suitable thermodynamic and transport property models for Novec<sup>TM</sup>649 by using a third-order finite volume solver [22]. The simulated range of Mach numbers,  $M \in [0.1, 0.95]$  includes the wind tunnel experimental conditions as well as transonic conditions with strong compressibility effects, resulting in drag divergence. The Reynolds numbers are the same as in the wind tunnel experiments. There, the boundary layer transitions over the surface, leading to a turbulent separation on the aft section of the cylinder. At the high Reynolds numbers of interest for the present parametric study, higher fidelity methods such as Large or Detached Eddy Simulation (LES/DES) are prohibitively expensive in terms of computing time. We thus recur to RANS equations despite their well-known inaccuracies in capturing details of boundary layer transition and separation [23, 24, 25]. We expect the solutions to be accurate enough to identify the main trends and to highlight the dense-gas effects. Furthermore, for periodic flows with a large separation of flow scales, such as those considered in this study, the unsteady (U)RANS can improve predictions by resolving mean-field unsteady motions, in our case the periodic vortex shedding [26]. Consequently, URANS simulations are also reported in this study, providing an estimate of turbulence modelling uncertainties. More in general, few authors have investigated numerically cylinder flows at both high Mach and high Reynolds number [27], as well as cross-validated against experimental measurements [28], and all such studies are restricted to air as the working fluid. Nevertheless, the organic vapor flow in such configuration can drastically diverge from that of a perfect gas, depending on the chosen operating conditions. To the authors' knowledge, a study of non-ideal compressible gas flow over a circular cylinder in the said Reynolds number range and in transonic regime is essentially missing in the literature.

This study presents for the first time a systematic numerical investigation of the compressible Novec<sup>TM</sup>649 flow around a circular Pitot probe, along with detailed cross-validations of numerical results and experimental pressure measurements inside a wind tunnel at FH Münster. Furthermore, we also explore increasingly non-ideal freestream thermodynamic conditions and higher Mach numbers, not reached in the experiments, more representative of ORC turbomachine working conditions. Finally, we also assess the suitability of RANS/URANS models for predicting the base pressure of bluff bodies. The results are expected to be of interest for further investigations of dense gas flows in ORC turbines.

## 2. Experimental setup and numerical method

### 2.1. Wind tunnel experiments

Figure 1 shows the high subsonic wind tunnel CLOWT test section where the rotatable cylindrical Pitot tube is immersed. It is capable of using dense gas as a working fluid, and was built at FH Münster [20]. Specifically, the fluorinated ketone Novec<sup>TM</sup>649 is selected for the study of dense gas flows, due its practicability, low toxicity and inflammability, as well as high thermal stability. Some useful properties of the dense working fluid are given in Table 1. A static pressure sensor is mounted inside the cylindrical cage

$T_c$ [K]	$p_c$ [MPa]	$\rho_c$ [kg/m <sup>3</sup> ]	$\mathcal{M}$ [kg/mol]	$c_v(T_c)$ [J/kgK]	$R_g$ [J/kgK]
441.810	1.869	606.804	316.044	975.960	26.307

Table 1: Novec<sup>TM</sup>649 properties [29].

and is connected to the surface pressure tap (fig. 1). Because the tube and hole are small,  $D_{tube} = 5mm$  and  $D_{tap} = 0.5mm$  respectively, manufacturing uncertainties exist and might affect the flow. This aspect was taken into consideration throughout the study. Time averaged wall static pressure data was obtained for a range of operating conditions [20], summarised in table 2.

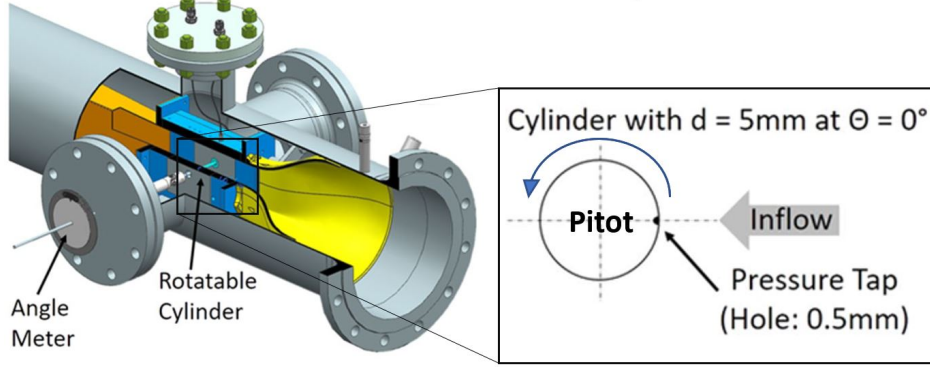


Figure 1: Closed Loop Organic vapor Wind Tunnel (CLOWT) at FH Münster [20]. (1.5 column, color)

Fluid	$p_{in}/p_c$	$\rho_{in}/\rho_c$	$Z_{in}$	$\Gamma_{in}$	$M_{in}$	$Re_{D,in}$	$\gamma_{in}$
Novec649 <sup>TM</sup>	0.079	0.026	0.940	0.983	0.650	$3.4 \times 10^5$	1.050
Novec649 <sup>TM</sup>	0.166	0.060	0.880	0.938	0.130	$1.0 \times 10^5$	1.050
Novec649 <sup>TM</sup>	0.166	0.060	0.880	0.938	0.410	$4.7 \times 10^5$	1.050
Novec649 <sup>TM</sup>	0.166	0.060	0.880	0.938	0.600	$6.1 \times 10^5$	1.050
Novec649 <sup>TM</sup>	0.166	0.060	0.880	0.938	0.950	$2.5 \times 10^5$	1.050*
Novec649 <sup>TM</sup>	0.553	0.200	0.870	0.852	0.650	$3.4 \times 10^5$	1.081*
Novec649 <sup>TM</sup>	0.884	0.400	0.700	0.732	0.650	$3.4 \times 10^5$	1.222*
Novec649 <sup>TM</sup>	0.948	0.600	0.500	0.578	0.650	$3.4 \times 10^5$	2.245*
Air			1.000	1.200	0.190	$1.1 \times 10^5$	1.400
Air			1.000	1.200	0.410	$4.7 \times 10^5$	1.400
Air			1.000	1.200	0.600	$6.1 \times 10^5$	1.400
Air			1.000	1.200	0.700–1.000	$2.5 \times 10^5$	1.400

Table 2: Entry operating conditions for experiments and simulations (marked \* were not measured experimentally).

## 2.2. Numerical method

We solve the two-dimensional compressible RANS equations for single-species non-reacting flow, written in integral form, by using an in-house structured finite-volume code, developed for dense gas flow computations [22]. The solver includes various thermodynamic and transport property models. In the present numerical campaign, the perfect polytropic gas law is used for air, and the polynomial equation of state of Peng-Robinson [30] corrected by Stryjek-Vera [31] was used to model the thermodynamic properties of Novec649<sup>TM</sup>, along with a power-law approximation of the specific heat in the dilute gas limit. For a PFG, dynamic viscosity  $\mu$  and thermal conductivity coefficient  $k$  are computed using the Sutherland law while for the dense gas these quantities are obtained through the Chung–Lee–Starling models [32]. The turbulent stresses are modelled by the Spalart–Allmaras one-equation model, which makes use of Boussinesq’s hypothesis for modelling the Reynolds stress tensor[33]. In the range of Reynolds numbers considered in the present study, the shear layers and the wake are expected to be fully turbulent, justifying the use of a RANS model. The ratio of span to diameter in the companion experiments is 10 so that the present 2D RANS simulations can be compared to measurements at mid-span.

A centered spatial discretization scheme of nominal third-order accuracy is used for the inviscid fluxes, and a second-order accurate approximation is used for the viscous fluxes. A non-linear artificial viscosity is implemented to insure numerical stability and to damp spurious oscillations caused by flow discontinuities. The time-marching algorithm is a four-stage Runge–Kutta scheme with implicit residual smoothing added at each stage to increase the maximum allowable CFL number. The reader is referred to [22] for more information about the numerical solver.

For the simulations reported in this study, we consider the unconfined flow past a 2D cylinder. For such external flow computations, characteristics boundary conditions are applied at far field boundaries, where the uniform free-stream conditions are assumed to be recovered. Turbulence intensity at the inlet is assumed to be negligible. The no-slip condition is enforced at the wall, which is assumed to be adiabatic (temperature derivative in the direction normal to the wall is set to zero).

Numerical simulations were conducted at various thermodynamic entry conditions and Mach and Reynolds numbers, as listed in Table 2, including those investigated in CLOWT experiments. Selected operating points are represented in the Clapeyron diagram given in figure 2. The black solid and light grey

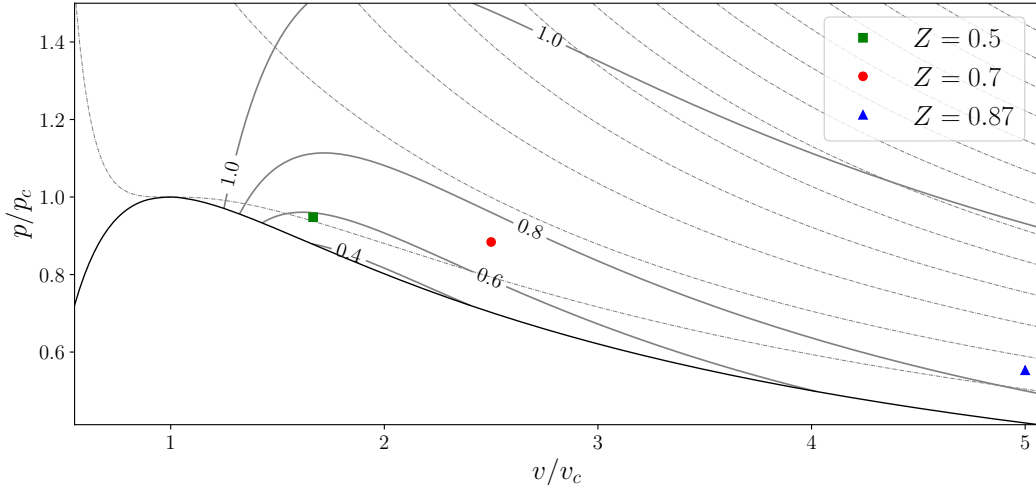


Figure 2: Novec649<sup>TM</sup> pressure-volume space obtained with the Peng-Robinson-Stryjek-Vera equation of state. Thick black line: coexistence curve; thin black lines with inlines: iso- $\Gamma$  contours; thin grey lines: isotherms (**double column, color**)

dashed lines correspond to  $\Gamma$  and reduced temperature  $T_r = T/T_c$  iso-contours respectively, where  $T_c$  is the critical temperature.

In all of the simulations, the boundary layer is fully discretized with  $\Delta n^+ \approx 1$ -2 for the highest Reynolds number case ( $\Delta n^+$  being the size of the first cell off the wall in the wall-normal direction  $n$ , expressed in wall units), i.e.  $Re_D = 6.1 \times 10^5$ , resulting in  $(\Delta n)_1/D \approx 10^{-4}$ . In the case of steady RANS computation, we define the circumferential cell distribution from the wall cell height as  $\Delta t^+/\Delta n^+ \approx 1000$  (with  $\Delta t^+$  the azimuthal mesh spacing in wall units). To reduce the effects of boundary conditions, we make the domain large  $[-20D; 30D]$  and  $\pm 10D$  in the streamwise and transverse directions respectively. Three multi-block structured curvilinear grids were made to assess the solution convergence. Their respective resolutions are given in Table 3, where the total number of cells  $N_{\text{cells}}$ , first cell height  $(\Delta n)_1/D$  and number of cells  $N_\theta$  in the azimuthal direction are given. Each grid is made of 5 blocks: one 'O' block around the cylinder and

Grid	$N_{\text{cells}}$	$(\Delta n)_1/D$	$N_\theta$	$C_d$
A	25,888	$1.0 \times 10^{-4}$	80	0.897
B	35,648	$5.0 \times 10^{-5}$	80	0.884
C	50,326	$5.0 \times 10^{-5}$	160	0.877

Table 3: Grid refinement level.

four 'H' blocks to connect to the domain limits. The upper half of a close-up view of the cylinder is given in figure 3. We then simulate the Novec<sup>TM</sup>649 flow at  $M_{in} = 0.6$  and  $Re_D = 6.1 \times 10^5$  on all grids using the RANS method. Figure 4 shows the  $\Delta y^+$ , friction coefficient  $C_f$  and pressure coefficient  $C_p = \frac{p - p_{in}}{p_0 - p_{in}}$  ( $p_0$  being the upstream total pressure) evolution on the cylinder surface against angular coordinate  $\theta$  in degrees.

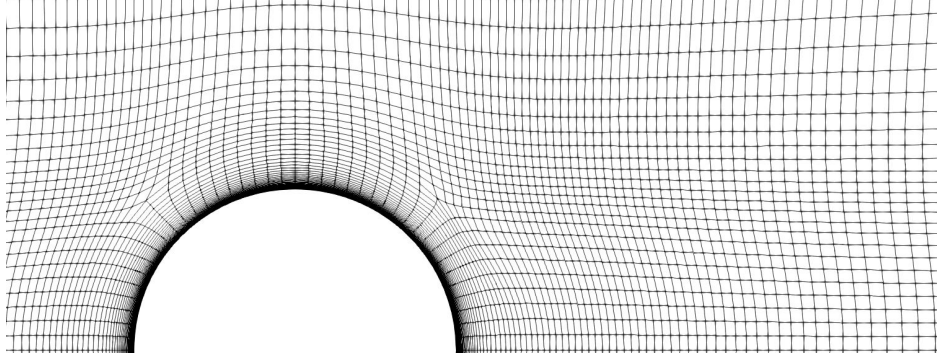


Figure 3: Grid details. (1.5 column)

The pressure drag coefficient  $C_d$  is obtained for each computation as:

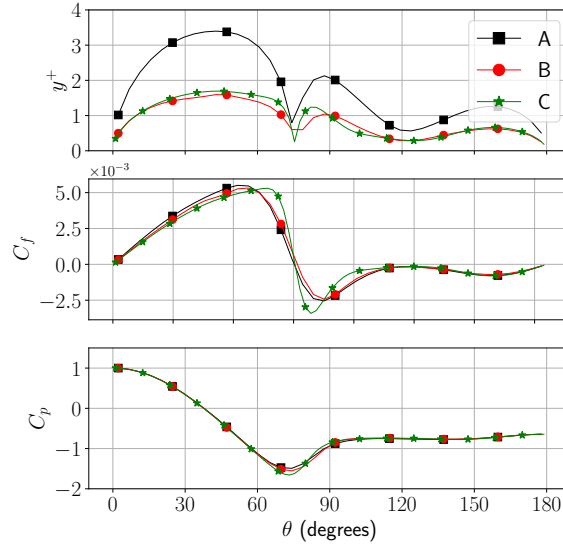


Figure 4: Wall spacing  $\Delta y^+$ , friction coefficient  $C_f$  and pressure coefficient  $C_p$  for grids A, B and C at  $M = 0.6$ ,  $Re_D = 6.1 \times 10^5$ . (1. column, color)

$$C_d = \int_{\pi}^0 C_p(\theta) d \sin \theta \quad (3)$$

and it is reported in Table 3 for each computation. Drag coefficient variations between all meshes stay within 2%. Overall, Mesh A was retained for steady computations as the solution only varies very slightly as shown by the  $C_f$  and  $C_p$  evolutions. For unsteady (U)RANS, an additional grid with  $y_1/D = 1.0 \times 10^{-4}$  and  $N_\theta = 160$ , i.e twice more refined only in the tangential direction to the wall, was adopted to better describe the von Kàrmàn street. The solution residuals were reduced by at least five orders of magnitude for the steady computations. The unsteady solutions were advanced in time with a time step corresponding to approximately 1/100 of the shedding period. After an initial transient of  $\sim 10$  periods, time averaging was started over an interval of more than 75 vortex shedding periods. To avoid long transient regimes in unsteady computations, the RANS solution was used to initialise the flow field for the URANS calculation.



### 3. Results and discussion

Time averaged Mach fields and streamlines of the Novec™649 flow for increasing inlet Mach number at constant compressibility factor  $Z_{in} = 0.88$ , simulated with both RANS and URANS methods are reported in figure 5. In every case a symmetric recirculation bubble has developed on the aft section of the cylinder,

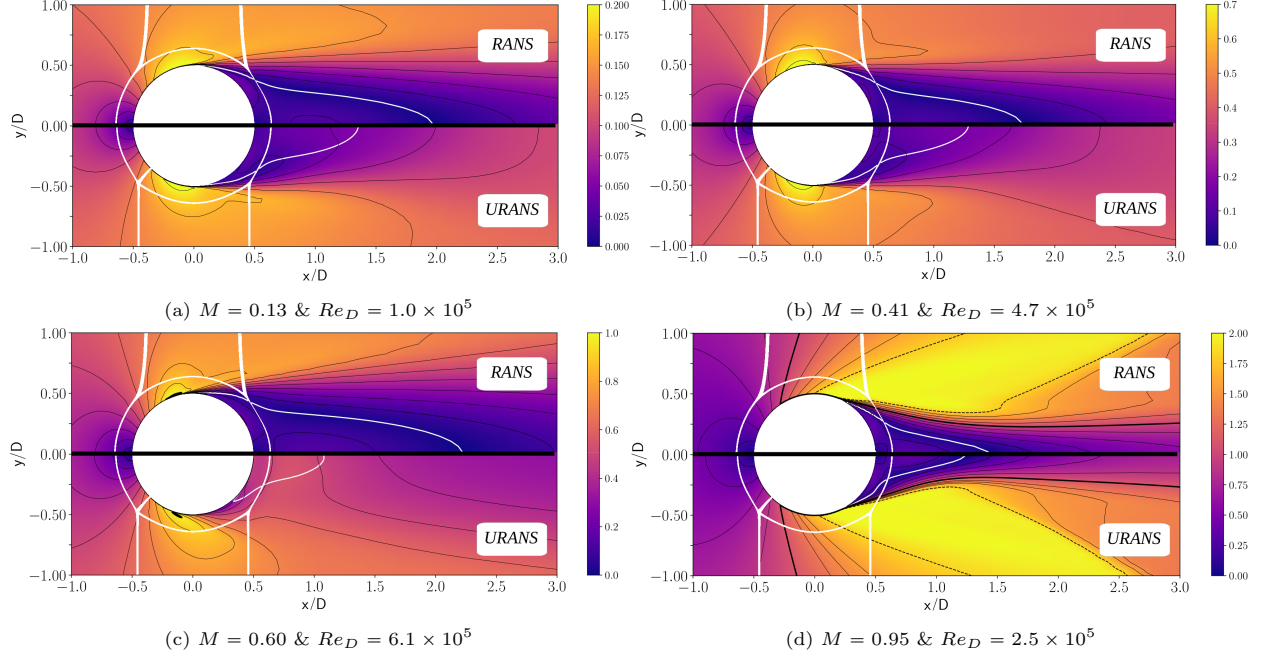


Figure 5: Isocontours of the Mach number of RANS and URANS solutions for  $Z_{in} = 0.88$  and different inlet conditions. The black dotted line highlights the sonic line  $M = 1$ . The white line corresponds to zero longitudinal velocity,  $u_x = 0$ . **double column, color**

visualized in the plot by the  $u_x = 0$  contour (white line), formed by two counter rotating vortices. The recirculation length  $L_r$  varies significantly with the Mach number. Thick black curves correspond to the  $M = 1$  isocontour and delimitate the supersonic regions, while black dotted curves correspond to the shock waves' Mach number isocontour. In the RANS solutions,  $L_r$  decreases from  $M_{in} = 0.13$  to  $M_{in} = 0.41$  as a result of the delayed boundary layer separation, due to the more favorable local pressure gradient. When  $M = 0.60$  the maximum Mach number reached is  $M_{max} \approx 1.1$  and a small supersonic region exists near the suction peak. The presence of a shock wave may lead to premature boundary layer separation, resulting in a thicker wake and longer recirculation bubble. When the inlet Mach number is further increased up to  $M_{in} = 0.95$ , the wake becomes bounded by shock waves on the aft section of the cylinder. When the shear layers meet approximately  $1D$  downstream the cylinder, oblique shock waves are generated. In the URANS simulated flows,  $L_r$  remains approximately constant from  $M_{in} = 0.13$  to  $M_{in} = 0.41$ , however the supersonic region predicted for the case  $M_{in} = 0.60$  is more extended compared to the RANS computation, leading to a supersonic expansion and a shorter bubble behind the cylinder. Thus, the consideration of unsteady events with the URANS method strongly affects the computational results in this regime. Interestingly, the same flow topology as for the steady computation is obtained at  $M_{in} = 0.95$ , showing that these conditions make the wake quasi-stationary and independent of unsteady phenomena, as observed by [28] in the case of a perfect gas flow.

We plot the pressure coefficient  $C_p$  evolution on the cylinder surface in figure 6 against angular position  $\theta$  in degrees, obtained by both RANS and URANS methods, for air and Novec™649 at various subsonic freestream conditions against experimental measurements from [20]. We see in figure 6 that the ideal



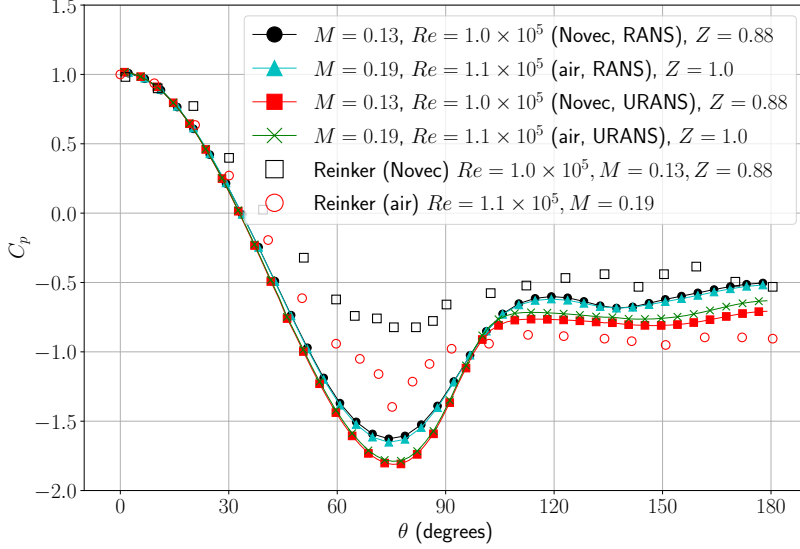


Figure 6:  $C_p$  evolution vs.  $\theta$  for flows at Mach  $\sim 0.1 \div 0.2$ . **1.5 column, color**

and dense gas flow RANS computations yield nearly superimposed  $C_p$  evolutions, showing that the flow field does not exhibit significant non-ideal gas effects at these conditions. The same can be established for the URANS solutions. Moderate deviations between the two methods are seen in the minimum  $C_p$  and separated flow regions, which can be attributed to residual uncertainties in time averaging. However, significant discrepancies between the air and Novec<sup>TM</sup>649 pressure measurements exist. The minimum  $C_p$  for air is much lower than for the organic vapour, hence the lower separated flow pressure. While the numerical back pressure is comprised within the scatter of experimental data and turbulence modelling errors exist, we attribute the large differences between air and Novec<sup>TM</sup>649 to measurement uncertainties. Indeed, measurements in the considered range of Reynolds numbers are very sensitive to geometry defects, which exist on the tube; their effect can be seen for angles  $\theta \in [60^\circ; 90^\circ]$ , where the  $C_p$  evolution does not follow either smooth or rough cylinder data [20, 34]. On the other hand, figure 7 shows very good agreement between measured and URANS  $C_p$  distributions at Mach 0.41, for both Novec<sup>TM</sup>649 and air [20, 35]. At these conditions, still no strong dense gas effects are reported and the flow is mostly driven by the Reynolds number. At these conditions, both RANS and URANS simulations capture well the experimental data. In figure 8 are reported the  $C_p$  evolutions for freestream conditions corresponding to Mach 0.60-0.65, showing that URANS is in much better agreement with experimental data than RANS. While the peak suction pressure is reasonably well captured, the back pressure coefficient  $C_{p,b} = C_p(180^\circ)$  found in the RANS simulations is largely overestimated. This is linked to figure 5c where we showed the capital role of unsteadiness on the simulation results: URANS partly accounts for increased wake mixing and momentum transport, leading to a shorter recirculation bubble that in turn induces a lower  $C_{p,b}$ . In the case of incipient transonic flow, this seems to improve the agreement between numerical data and wind tunnel measurements, even though flow visualisations would be needed to confirm this point.

Pressure distributions are integrated to obtain the pressure drag coefficients as a function of Mach number. The results from RANS and URANS simulations are compared with the measurements in CLOWT in Figure 9, of which the inlet conditions are given in Table 2, along with other published data. At low values of the Mach number (up to 0.5), the drag is strongly dependent on the Reynolds number. It slightly increases from 1.2 at low Re (see measurement points for air), whereas a sharp fall and rise, corresponding to the critical range of Reynolds numbers (drag crisis), is present for Novec<sup>TM</sup>649 flow. Around  $M_{in} \approx 0.1-0.2$ ,

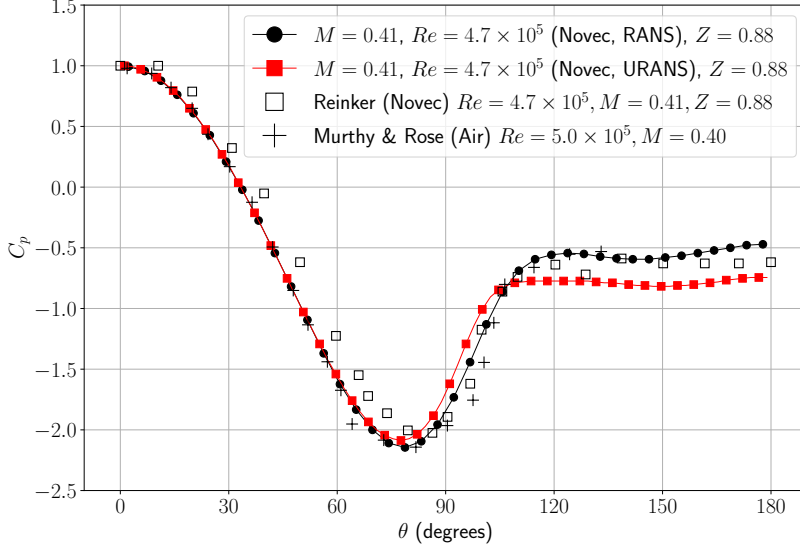


Figure 7:  $C_p$  evolution vs.  $\theta$  for flows at Mach  $\sim 0.4$ . **1.5 column, color**

a fair agreement is obtained between both RANS and URANS and experiments. For  $M=0.4$  conditions, the drag value has been found to be sensitive to flow details such as surface roughness and stream turbulence. The agreement between simulations and experiments remains satisfactory. Compressibility effects come into play at  $M=0.6$  accompanied by a drag increase in accordance with previous cylinder databases in air. At higher velocities, URANS are in very good agreement with the in flight measurements of Welch [17], and fall within the dispersion of other experimental data [16, 35, 19], whereas RANS fails to capture the base pressure and yields an underestimation of the mean drag. The drag-divergence arises for transonic Mach numbers greater than 0.8 and is well reproduced by URANS simulations in air. In such region, shock waves appear that are strongly dependent on gas properties, and the deviation between Air and Novec<sup>TM</sup>649 results becomes larger. At this regime, drag coefficients are higher for Novec<sup>TM</sup>649 than in air. This is because of the considerably lower values of  $C_{p,min}$  reached in the more compressible organic gas, resulting in turn in lower values of the base pressure and increased form drag. The latter is preponderant with respect to wave drag for the present bluff body flow and range of Mach numbers.

### 3.1. Strongly non-ideal gas flow

To investigate the role of dense gas effects on the cylinder aerodynamics, we explore increasingly non-ideal thermodynamic freestream conditions numerically with fixed Mach and Reynolds number  $M_{in} = 0.65$  &  $Re_D = 3.5 \times 10^5$ . Table 2 summarises the inlet quantities, where conditions marked \* are shown in the Clapeyron diagram in figure 2. Since we are mostly interested in thermodynamic effects, and to reduce computational cost of the parametric study, we use the RANS method to simulate the Novec<sup>TM</sup>649 flows. The pressure coefficients are reported in figure 10, and the fundamental derivatives of gas dynamics  $\Gamma$  on the cylinder surface are given in figure 11.

For perfect to weakly non-ideal gas behaviour ( $Z \geq 0.88$ ) the  $C_p$  curves are almost superimposed and show only very slight effect of non-ideal thermodynamics. Indeed, the corresponding  $\Gamma$  from figure 11 show little deviation from the inlet values given in table 2, even though  $\Gamma < 1$  everywhere. When  $Z$  is further decreased, the minimum  $C_p$  decreases accordingly as a result of the larger compressibility of the organic vapour. This is linked to the value of  $\Gamma$  which is moving well below unity (figure 11), showing that the speed of sound exhibits a more severe non-ideal behavior across the flow. However, in the range of Mach

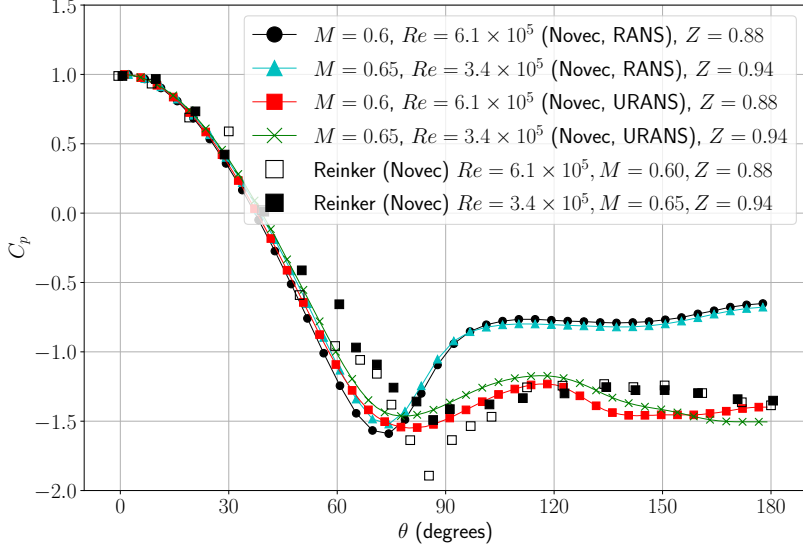


Figure 8:  $C_p$  evolution vs.  $\theta$  for flows at Mach  $0.6 \div 0.65$ . **1.5 column, color**

numbers and thermodynamic conditions studied, deviations in the minimum  $C_p$  remain below  $\approx 13\%$ . For  $0.7 \lesssim Z \leq 1$ , we attribute these differences mostly to the value of the isentropic exponent, given in table 2, which essentially drives the compressibility of gas. Non-ideal gas effects start to be important below  $Z = 0.7$ .

#### 4. Conclusions

The compressible organic vapour flow past a circular cylinder was investigated numerically to complement the experimental pressure measurements made in a closed-loop dense gas wind tunnel CLOWT [20] and expand it to more severe non-ideal conditions. The geometry corresponds to a cylindrical Pitot tube immersed in a Novec™649 flow. Both steady and unsteady flow computations were performed and cross-validated to get insight into dense-gas effects on Pitot probe devices for such gases and to estimate potential losses associated with the viscous wake from a rounded trailing edge typical of turbine blade. The study also allowed, for the first time in the literature, to cross-validate numerical results with available experiments at Mach numbers up to 0.6 and mildly non-ideal conditions. The following conclusions can be drawn:

1. For the weakly non-ideal conditions reported experimentally, the numerical results show no effect of non-ideal thermodynamic behaviour of the organic vapour on the flow, as the minimum fundamental derivative reached is  $\Gamma_{\min} \approx 0.92$  which is close to unity. Hence, the deviations in experimental data are attributed to geometrical inaccuracies of the Pitot tube which cause measurement deviations, especially in the critical Reynolds range studied.
2. We found that the consideration of unsteady phenomena by the URANS method leads to a better reproduction of the experimental data for incipient transonic flows compared to the RANS method. In steady computations, the recirculation bubble is consistently larger than in URANS with a factor larger than 2 for the transonic inlet conditions  $M = 0.6$  &  $Re_D = 6.1 \times 10^5$ . This causes the back pressure to be systematically overpredicted by up to 45% (figure 8), and the drag coefficient to be underestimated.
3. Increasingly non-ideal thermodynamic conditions, not tested in the experimental facility, were explored numerically to complement the experiments and to investigate the effects of real gas behaviour on the

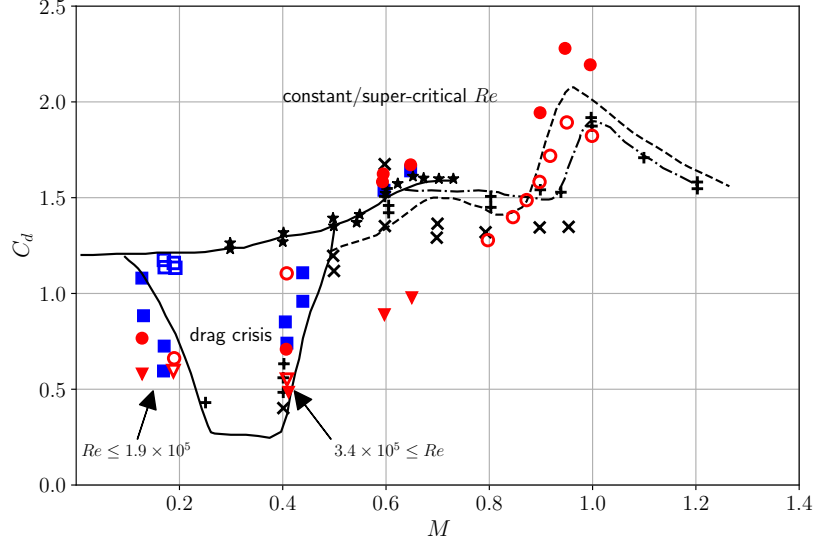


Figure 9: Evolution of the drag coefficient  $C_d$  vs. the Mach number. ● present URANS, Novec<sup>TM</sup>649; ○ present URANS, air; ▼ present RANS, Novec<sup>TM</sup>649; ▽ present RANS, air; ■ experiments of Reinker *et al.* [20], Novec<sup>TM</sup>649; □ experiments of Reinker *et al.* [20], Air; — data from various experiments from [36], both in the sub- and super-critical regimes; - - data from flight tests of Welsh [17]; - · - mean line through data of Macha [16]; \* experiments of Gowen & Perkins [18]; + experiments of Murthy & Rose [35]; × experiments of Ackerman *et al.* [19]; **1.5 column, color**

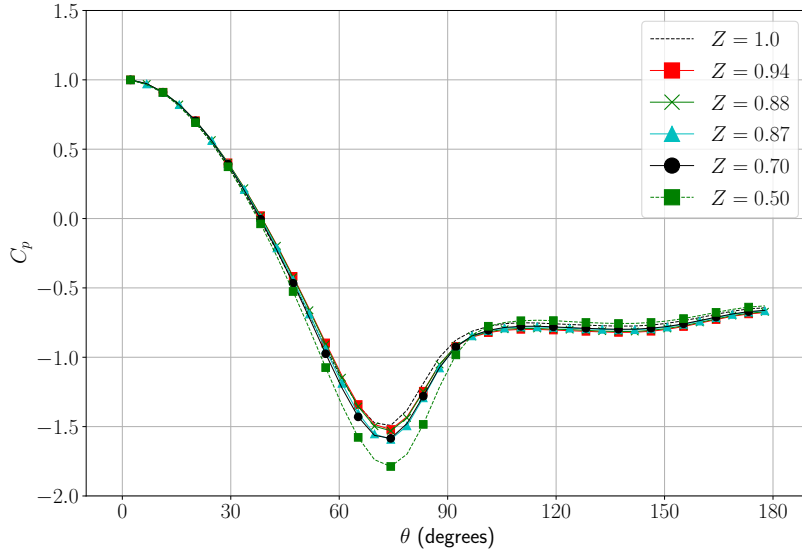


Figure 10:  $C_p$  evolution vs.  $\theta$  of increasingly non-ideal thermodynamic conditions at  $M = 0.65$  &  $Re_D = 3.5 \times 10^5$ . **1.5 column, color**

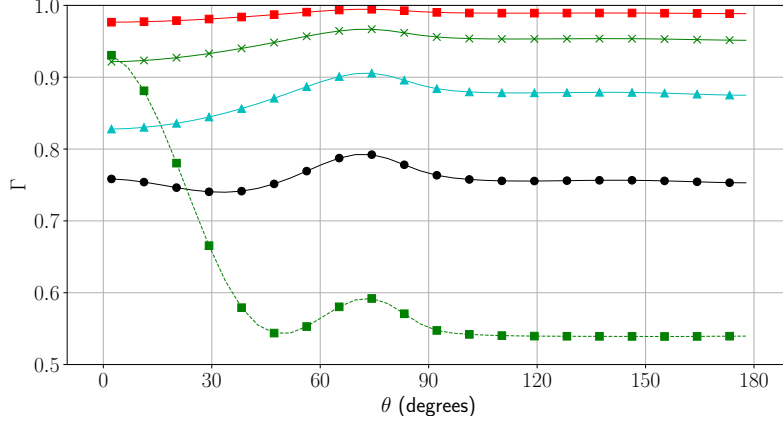


Figure 11:  $\Gamma$  evolution vs.  $\theta$  of increasingly non-ideal thermodynamic conditions at  $M = 0.65$  &  $Re_D = 3.5 \times 10^5$  (legends identical to figure 10.1.5 **column, color**)

flow around the cylinder, at high subsonic conditions. Stronger dense gas effects cause the vapour to expand more at the suction peak, reducing the minimum pressure reached on the cylinder by 17% in the most non-ideal configuration.

4. For sufficiently diluted operating thermodynamic conditions, i.e. for compressibility factor in the range  $0.7 < Z < 1$ , non-ideal gas effects are weak and differences observed between air and Novec at high-subsonic and transonic Mach numbers are mostly attributed to the different isentropic exponent  $\gamma$  of the two gases. However, this is not the case when  $Z \leq 0.7$ . As such conditions, non-ideal gas effects lead to increased compressibility and more significant deviations of the pressure distributions for freestream Mach numbers as low as 0.6.

In future work, higher fidelity computational methods will be employed such as Large Eddy Simulation to better represent the wake flow at the present challenging Reynolds number conditions, and quantify the effects of dense gas behaviour on turbulent structures. Moreover, the compressible dense gas flow around small-diameter cylinders, representative of a hot-wire anemometer, will be investigated both numerically and experimentally to support the calibration of such measuring devices.

### Declaration of competing interest

The authors declare that they have no known competing financial interests or personal relationships that could have appeared to influence the work reported in this paper.

### Acknowledgements

This study is part of the international project REGAL-ORC co-funded by the ANR (grant S20JRAR055) in France and DFG in Germany. This work was granted access to the HPC resources of IDRIS and TGCC under the allocations A0092A01736 and A0122A13457 made by GENCI (Grand Equipement National de Calcul Intensif).

## Nomenclature

### *Acronyms*

CFD	Computational Fluid Dynamics
CFL	Courant-Friedrichs-Lewy number
PFG	Perfect Gas
RANS	Reynolds Averaged Navier-Stokes
URANS	Unsteady Reynolds Averaged Navier-Stokes

### *Symbols*

$c$	speed of sound
$c_v$	specific heat at constant volume
$c_p$	specific heat at constant pressure
$C_d$	pressure drag coefficient
$C_f$	friction coefficient
$C_p$	pressure coefficient
$C_{p,b}$	back pressure coefficient
$L_r$	recirculation length
$D$	cylinder diameter
$k$	thermal conductivity
$M$	Mach number
$\mathcal{M}$	molar mass
$p$	static pressure
$Re$	Reynolds number
$s$	entropy
$T$	temperature
$U$	freestream velocity
$v$	specific volume
$x, y$	Cartesian coordinates
$Z$	compressibility factor

### *Subscript/superscript*

$c$	critical conditions
$in$	freestream inlet conditions
$r$	reduced properties (normalized by critical ones)
$0$	total conditions
$+$	wall quantities

### *Greek symbols*

$\gamma$	isentropic exponent
$\Gamma$	fundamental derivative of gas dynamics
$\mu$	dynamic viscosity
$\theta$	angular location on cylinder surface
$\rho$	fluid density

## Credit authorship contribution statement

Camille Matar: Conceptualization, Simulations, Analysis, Writing - original draft; Paola Cinnella: Supervision, Conceptualization, Simulations, Analysis, Writing - review & editing, Funding acquisition; Xavier Gloerfelt: Analysis, Writing - review & editing; Felix Reinker: Experiments, Analysis; Stefan aus der Wiesche: Project administration, Experiments, Funding acquisition.



## References

- [1] E. Rinaldi, R. Pecnik, P. Colonna, Unsteady operation of a highly supersonic organic Rankine cycle turbine, *Journal of Turbomachinery* 138 (12) (2016) 121010.
- [2] A. P. S. Wheeler, J. Ong, The role of dense gas dynamics on organic Rankine cycle turbine performance, *Journal of Engineering for Gas Turbines and Power* 135 (10) (2013) 102603.
- [3] P. A. Thompson, A fundamental derivative in gas dynamics, *Physics of Fluids* 14 (9) (1971) 1843–1849.
- [4] J.-C. Hoarau, P. Cinnella, X. Gloerfelt, Large eddy simulations of strongly non ideal compressible flows through a transonic cascade, *Energies* 14 (3) (2021) 772–1–772–20.
- [5] H. Bethe, On the theory of shock waves for an arbitrary equation of state, *Classic Papers in Shock Compression Science* (1998) 421–495.
- [6] D. Baumgärtner, J. Otter, A. Wheeler, The effect of isentropic exponent on transonic turbine performance, *Journal of Turbomachinery* 142 (2020) 081007–1–081007–10.
- [7] G. Otero, S. Smit, R. Pecnik, Three-dimensional unsteady stator-rotor interactions in high-expansion organic Rankine cycle turbines, *Energy* 217 (2021) 119339.
- [8] N. Anand, P. Colonna, M. Pini, Design guidelines for supersonic stators operating with fluids made of complex molecules, *Energy* 203 (2020) 117698.
- [9] E. Bufl, P. Cinnella, Preliminary design method for dense-gas supersonic axial turbine stages, *Journal of Engineering for Gas Turbines and Power* 140 (11) (2018) 112605.
- [10] N. Razaaly, G. Persico, P. Congedo, Impact of geometric, operational, and model uncertainties on the nonideal flow through a supersonic ORC turbine cascade, *Energy* 169 (2019) 213–227.
- [11] G. Cammi, C. Conti, A. Spinelli, A. Guardone, Experimental characterization of nozzle flow expansions of siloxane MM for ORC turbines applications, *Energy* 218 (2021) 119249.
- [12] M. Zocca, A. Guardone, G. Cammi, F. Cozzi, A. Spinelli, Experimental observation of oblique shock waves in steady non-ideal flows, *Experiments in Fluids* 60 (2019) 101.
- [13] G. Gori, M. Zocca, G. Cammi, A. Spinelli, P. Congedo, A. Guardone, Accuracy assessment of the Non-Ideal Computational Fluid Dynamics model for siloxane MDM from the open-source SU2 suite, *European Journal of Mechanics-B/Fluids* 79 (2020) 109–120.
- [14] J. Gerrard, The mechanics of the formation region of vortices behind bluff bodies, *Journal of Fluid Mechanics* 25 (1966) 401–413.
- [15] C. Sieverding, M. Manna, A review on turbine trailing edge flow, *International Journal of Turbomachinery Propulsion and Power* 5 (2020) 10.
- [16] J. Macha, Drag of circular cylinders at transonic Mach numbers, *AIAA Journal* 14 (6) (1977) 605–907.
- [17] C. Welsh, The drag of finite-length cylinders determined from flight tests at high Reynolds numbers for a Mach number range from 0.5 to 1.3, *Technical Note 2941, NACA* (1953).
- [18] F. Gowen, E. Perkins, Drag of circular cylinders for a wide range of Reynolds numbers and Mach numbers, *Technical Note 2960, NACA* (1953).
- [19] J. R. Ackerman, J. P. Gostelow, A. Rona, W. E. Carscallen, Base Pressure Measurements on a Circular Cylinder in Subsonic Cross Flow, *AIAA*.
- [20] F. Reinker, L. Wagner, R. and Hake, S. aus der Wiesche, High subsonic flow of an organic vapor past a circular cylinder, *Experiments in Fluids* 62 (2021) 54.
- [21] J. Wyler, Probe blockage effects in free jets and closed tunnels, *Journal of Engineering Gas Turbines Power* 97 (4) (1975) 509–514.
- [22] P. Cinnella, P. Congedo, Numerical solver for dense gas flows, *AIAA Journal* 43 (11) (2005) 2457.
- [23] A. Travin, M. Shur, M. Strelets, P. R. Spalart, Detached-eddy simulations past a circular cylinder, *Flow, Turbulence and Combustion* 63 (2000) 293–313.
- [24] P. Catalano, M. Weng, G. Iaccarino, P. Moin, Numerical simulation of the flow around a circular cylinder at high Reynolds numbers, *International of Heat and Fluid Flow* 24 (4) (2003) 463–469.
- [25] K. Abdol Hamid, A. Elmilgui, S. Massey, S. Pao, Numerical study of flow past a circular cylinder using RANS, hybrid RANS/LES and PANS formulations, in: *22nd Applied Aerodynamics Conference and Exhibit, Vol. AIAA 2004-4959*, Providence, Rhode Island, 2004.
- [26] A. J. Hillis, J. Zang, R. M. Stringer, Unsteady RANS computations of flow around a circular cylinder for a wide range of Reynolds numbers, *Ocean Engineering* 87 (2014) 1–9.
- [27] Z. Xia, Z. Xiao, Y. Shi, S. Chen, Mach number effect of compressible flow around a circular cylinder, *AIAA Journal* 54 (6) (2016) 2004.
- [28] C. Xu, L. Chen, X. Lu, Effect of Mach number on transonic flow past a circular cylinder, *Chinese Science Bulletin* 54 (2009) 1886–1893.
- [29] 3M, Novec 649 Engineered fluid (2009).
- [30] D.-Y. Peng, D. Robinson, A new two-constant equation of state, *Industrial and Engineering Chemistry Fundamentals* 15 (1) (1976) 59–64.
- [31] R. Stryjek, J. H. Vera, PRSV: An improved Peng–Robinson equation of state for pure compounds and mixtures, *The Canadian Journal of Chemical Engineering* 64 (2) (1986) 323–333.
- [32] T. Chung, M. Ajlan, L. Lee, K. Starling, Generalized multiparameter correlation for nonpolar and polar fluid transport properties, *Industrial and Engineering Chemistry Fundamentals* 27 (4) (1988) 671–679.
- [33] P. Spalart, S. Allmaras, A one-equation turbulence model for aerodynamic flows, *La Recherche Aéronautique* 1 (1994) 5–21.

- [34] E. Achenbach, Distribution of local pressure and skin friction around a circular cylinder in cross-flow up to  $Re = 5 \times 10^6$ , *Journal of Fluid Mechanics* 34 (4) (1968) 625–639.
- [35] V. Murthy, W. Rose, Detailed measurements on a circular cylinder in cross flow, *AIAA Journal* (6) 549–550.
- [36] L. H. Jorgensen, A method for estimating static aerodynamic characteristics for slender bodies of circular and noncircular cross section alone and with lifting surfaces at angles of attack from  $0^\circ$  to  $90^\circ$ , Technical Note TN O-7228, NASA (1973).